PHYSICAL REVIEW E **75**, 066109 (2007)

Simulation of the hydraulic fracture process in two dimensions using a discrete element method

Sergio Andres Galindo Torres* and Jose Daniel Muñoz Castaño†
Physics Department, Universidad Nacional de Colombia, Bogotá, Colombia
(Received 1 October 2005; revised manuscript received 13 April 2007; published 26 June 2007)

We introduce a discrete element simulation for the hydraulic fracture process in a petroleum well which takes into account the elastic behavior of the rock and the Mohr-Coulomb fracture criterium. The rock is modeled as an array of Voronoi polygons joined by elastic beams, which are submitted to tectonical stresses and the hydrostatic pressure of the fracturing fluid. The fluid pressure is treated like that of a hydraulic column. The simulation reproduces well the time and dimensions of real fracture processes. We also include an analysis of the fracturing fluid loss due to the permeability of the rock which is useful in an efficiency analysis of the treatment. The model is a first step for future applications in the petroleum industry.

DOI: 10.1103/PhysRevE.75.066109 PACS number(s): 46.50.+a, 47.85.Dh, 62.20.Mk, 07.05.Tp

I. INTRODUCTION

The hydraulic fracture is a commonly used method for increasing the output of a petroleum reservoir. In this process, water or some other fluid is injected into the well at a very high pressure at a constant flow rate. Because of the accumulation of fluid in the well bottom, the pressure begins to increase, and suddenly a crack in the reservoir's rock opens. The fluid pressure grows almost linearly in time before the crack opens, and begins to fluctuate once the fracture propagates into the reservoir [1]. This fluctuation can be measured at the surface by the engineers, and it is a clear indication of the evolution of the fracture. There are two important points in the function pressure vs time. The first one is the ISIP point (instantaneous shut in pressure) that takes place once the fluid injection is suspended. The fluid pressure continues to open the fracture while the tectonical stresses tend to close it. The second one is when the system reaches the equilibrium between these two forces, as can be seen in Fig. 1. When the equilibrium is reached, the fluid pressure equals the minimum *in situ* stress. Therefore, the hydraulic fracture gives us information about the stress state of the reservoir.

This stress state plays an important role in the geometry of the fracture. The crack tends to be normal to the direction of minimum stress, since it is easier to fracture the rock in this direction. If the difference between the two principal stresses in the horizontal plane is large, we can obtain a narrow and well-defined fracture; if the difference is small, the fracture is disperse and does not have a preferred direction. When one principal stress is smaller than the other two, or its value lies between them and in addition the maximal stress is high enough, the fracture mainly propagates on a plane, i.e., it is two dimensional [1]. This is the case of interest for our study. Actually, many models used in the petroleum industry (particulary the Penny-Kern model, which assumes the fracture as an ellipse, as explained below) take a fixed height of 0.3 to 1 m for fractures of a few hundred meters long [2], i.e., they are two dimensional.

Several attempts have been done to model the hydraulic fracture. These attempts can de divided into two different branches: macroscopical and microscopical models. The macroscopical models are widely used in the present petroleum engineering. They assume a simple geometry for the fracture (i.e., the fracture is elliptical or a rectangular box or some other simple geometrical entity [3]). The crack grows with the fluid pressure, but the general shape of the fracture is the same. The mathematics involved in these models are complex, but the computations associated with them are rather efficient in terms of time [3]. In contrast, microscopical models closely describe physical interactions, but computational effort is extremely large, since the rock is divided in many discrete elements and the computational complexity grows very fast with the number of elements. These models have been used by physicists for the study of fracture propagation in different scenarios, like soils [4] and collision fractures [5]. For the last quarter of the 20th century these models were barely used in petroleum engineering, since their application needed a high performance computer, not a

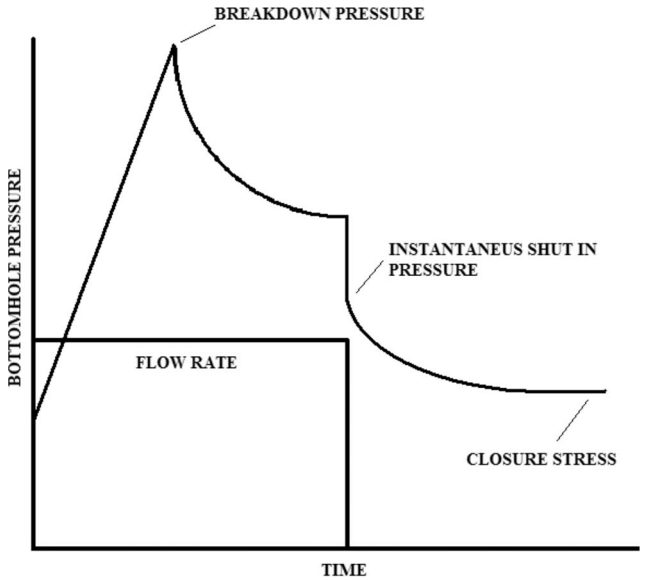

FIG. 1. A typical pressure behavior for a microhydraulic fracturing test of the *in situ* stress.

*sagalindot@unal.edu.co
†jdmunozc@unal.edu.co

simple PC. But since computers are more and more powerful each year, these microscopical models can be run on PCs of the present and its practical application may be closer than we think.

The objective of this work is to introduce a microscopical model to simulate the hydraulic fracture process with a propagation in a two-dimensional (2D) plane (provided that the *in situ* stress regime allows this constraint). The rock is divided into an array of Voronoi polygons that are bounded by elastic beams. If some threshold strain is overcome, the beam breaks. The water acts as a hydrostatic pressure that pushes all grains in contact with it. Tectonical stresses are represented by four rectangular elements that push the polygons together. The model gives good results with medium resolutions and small computational resources. Sections II and III explain how the rock and the fluid are modeled, respectively. The results for different tectonical stresses are shown in Secs. IV and V, and they are followed by the conclusions in Sec. VI.

II. THE ROCK

In order to model the rock, we based it on a model used for the fragmentation of colliding objects [5] that we will explain in detail below. Our contribution is to apply this model to the particular problem of the hydraulic fracture. Since we are interested in two-dimensional fractures, our model is based on a bidimensional array of Voronoi polygons that represents the reservoir rock. The array is assumed to be 0.3 m thick in the third dimension, as the Penny-Kern model does, and this value will be used to determine the rock parameters from actual values for limestone. To construct the Voronoi polygons we need first a set of points randomly distributed on the plane, called the Voronoi points. For each point we can define the Voronoi polygon associated with it as the set of points in the plane that are closer to the given Voronoi point than to any other one. In other words,

$$V(p) = \{x | f_{\text{dist}}(x,p) < f_{\text{dist}}(x,q)\}, \tag{1}$$

where $V(p)$ is the Voronoi polygon associated to the Voronoi point p, q in any other Voronoi point and the function f_{dist} is the euclidian distance between two points in the plane. Of course, the boundaries of these polygons are lines that are equidistant to two Voronoi points, and the vertices of these polygons are equidistant to three Voronoi points. This feature provide us with an equation for the coordinates x, y for each vertices. With this array, we ensure a random possible path for the fracture propagation, without any of the special geometries that most macroscopical models assume [1]. In order to obtain an homogeneous granular size, we divide the space into a square lattice, and only one Voronoi point dwells in each square. Each polygon has three degrees of freedom: the two coordinates of the center of mass and the angular displacement from the equilibrium position (see Fig. 2).

Of course, since the rock is modeled by the Voronoi polygons, two adjacent polygons should maintain a cohesive force between them. This force is modeled by the presence of one beam that connects them together and depends on the elastic constants of the rock. The form of the forces between

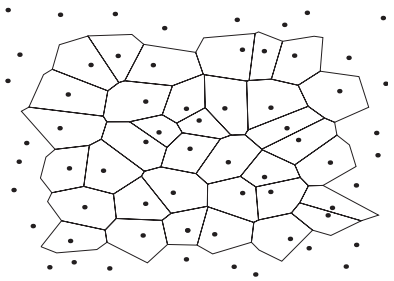

FIG. 2. A typical set of Voronoi polygons and points. If a line is drawn from one Voronoi point to another, this line will be perpendicular to the common side of the two corresponding Voronoi polygons.

two polygons i and j, used in the simulation is the following:

$$F_{ix} = \alpha_{ij}(x_j - x_i), \tag{2a}$$

$$F_{iy} = \beta_{ij}(y_j - y_i) + \frac{\beta_{ij} l_{ij}}{2}(\Theta_i + \Theta_j), \tag{2b}$$

$$M_i = \frac{\beta_{ij} l_{ij}}{2}(y_j - y_i + l_{ij}\Theta_j) + \delta_{ij} l_{ij}^2 (\Theta_j - \Theta_i), \tag{2c}$$

where the tensile force F_x has a direction perpendicular to the common side of the polygons, F_y is the shear force which is parallel to the common side, and the flexural torque M resists the *bending* of the cohesive beam. All of these quantities depend on the position of the center of mass of the ith polygon (x_i, y_i), its angular displacement from the x axis Θ_i (this x axis is perpendicular to the shared side), and the parameters $\alpha = 1/a$, $\beta = 1/(b + c/12)$, $\delta = \beta(b/c + 1/3)$, where $a = l/(EA)$, $b = l/(GA)$, and $c = l^3/(EI)$. Within these parameters, E is the tensile Young modulus, G is the shear modulus, A is the cohesive beam cross section (in our two-dimensional case, A is the length of the side that both polygons share times at fixed height h), and l is the length of the beam (the distance of equilibrium between the two center of masses). We assume the beam as a rectangular box with cross section A and length l. If the beam is bent, there is a plane in the middle of the box that does not change its length. Hence the moment of inertia for flexion I (i.e., the elastic resistance to the beam bending) is

$$I = \int z^2 dA, \tag{3}$$

with z the distance between the middle plane and the strained planes and dA is the beam cross-section differential. The integral is straightforward and gives us the formula $I = A^3/24h^2$ for every beam. This model has been used in several fracture problems [4] and it can be shown that it is a simple discretization of the continuous Cosserat equations [5].

In order to model the fracture process, we must introduce some fracture criterion. In our simulation we assume that there will be no further cohesive force between two adjacent

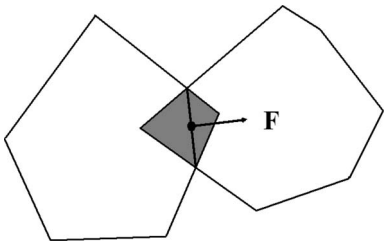

FIG. 3. Here we show the action of the granular repulsive force. The vertical line goes between the two points that define the intersection of the polygons. The force is perpendicular to this line, acts on the middle point of the line, and is proportional to the overlapping area between the polygons (in gray).

polygons when the strain overcomes a certain threshold. This criterion is ruled by the following conditions:

$$\varepsilon_t > t_t \text{ or } \varepsilon_s > t_s \text{ or } \max(\Theta_i, \Theta_j) > t_a, \tag{4}$$

with ε_t is the tensile and ε_s is the shear strain, Θ_i is the angular displacement mentioned above and t_t, t_s, t_a are the corresponding threshold values for the tensile strain, the shear strain, and the angular displacement. The threshold values are the same for every beam (1% in our simulations). The point here is that the beams between polygons are all different because of the Voronoi construction, which gives different sizes for each beam; therefore the threshold displacements for fracture are different, but they are not distributed by obeying any power law, at least *a priori*. The criterion is based on the Mohr-Coulomb theory of fracture [1], which states that the critical stress for the appearance of the fracture depends on the external stress applied to the rock.

When two Voronoi polygons intersect with each other, in addition, there appears an elastic repulsive force between them. This force is proportional to their overlapping area, is perpendicular to the line that joins the intersections of the two perimeters, and acts in the middle point of this line, as shown in Fig. 3. The exact value for this force is

$$\vec{F}_g = \frac{YA_{ol}}{L_c}\hat{\mathbf{n}}, \tag{5}$$

where Y is the granular Young modulus of the material, A_{ol} is the overlapping area, L_c is a characteristic length, given by $1/L_c = 0.5(1/r_i + 1/r_j)$ [4], where r_i is the radius of the circle with the same area of the ith polygon, and $\hat{\mathbf{n}}$ is a vector perpendicular to the dashed line in Fig. 3 with the repulsive sign.

However, all of these forces are conservative ones, and in absence of a dissipative mechanism, any initial perturbation in the system will generate an eternal oscillation of the polygons. So, a nonconservative force is needed in order to overcome this problem. We choose the simplest model for a viscosity force $\vec{F}_\mu$,

$$\vec{F}_\mu = -C\vec{V}, \tag{6}$$

where $\vec{V}$ is the velocity of the polygon and C is a viscosity constant. The C parameter was chosen by taking a single pair of two colliding grains and by asking that the frontal collision between two grains gives a speed reduction corresponding to a restitution coefficient of $e=0.8$ (a value which is usually considered reasonable for granular sand in oil engineering for several models and simulations [6]). The collision speed was chosen between 0.0015 and 0.0025 m/s, which are similar to those we found in our simulations. The restitution coefficient is taken as the ratio between the relative speeds after and before the collision of the two polygons, and we can determine these events when the overlapping area of Fig. 3 is zero. In general, C depends on the polygons shape and on the parameters that define the elastic repulsive force, but we did not find any significative dependence on the collision speed, at least for this small velocity range. We used a pair of polygons colliding, obtaining a value of $C = 1.622 \times 10^5$ N s/m (see Table I), which can be addressed as a first reasonable approximation to the dissipative forces.

TABLE I. Set of parameters used in our simulation.

Parameter	Value
Time step	0.0001 s
Rock density	3000 kg/m^3
Tensile Young modulus E	34.5 GPa
Shear Young modulus G	13.8 GPa
Granular modulus Y	69 GPa
Average length of a polygon side	2.1 m
Fixed height h of the fracture	0.3 m
Viscous friction coefficient C	1.622×10^5 N s/m
Value for the breaking thresholds	2%
Dynamic viscosity μ	1 cp
Permeability of the reservoir k	5 md

Finally we are interested in the behavior of the fracture geometry in the presence of the tectonical stresses. The external stresses are simply modeled as forces acting on rectangular polygons at the borders of the array (120 m large and 6 m width). In addition, these polygons feel the same repulsive force as the grains given by Eq. (5).

With these forces, the problem simplifies to the integration of the time equation for each polygon. This is done with the help of the molecular dynamics method [7]. In our simulation we chose the Verlet algorithm [8] to give the position of the particle in the next time step as follows $\mathbf{r}(t)$:

$$\mathbf{r}(t+\Delta t) = 2\mathbf{r}(t) - \mathbf{r}(t-\Delta t) + \mathbf{a}(t)\Delta t^2 + \mathbf{O}(\Delta t^4), \tag{7}$$

where Δt is the time step and $\mathbf{a}(t)$ is the acceleration of the desired polygon obtained by summing up all forces on the polygon and dividing by the mass. A similar equation holds for the angular displacements.

III. THE FLUID

Now we must proceed to model the fluid, which is the second half of the problem. Initially, the fluid enters into the rock with great pressure, but eventually there is a pressure

drop when the crack opens, since the volume that is occupied by the fluid starts growing. We will consider that the fluid pressure is normal to the fracture surface and we will ignore the shear force produced by the fluid viscosity.

Fluid viscosity is ignored as a damping force on the rock grains, because it is much smaller than the dissipative force between them. Actually, the only polygons affected by this force are those in contact with the fracture. By assuming a laminar flux on the surface in contact with the fluid, the total force on the surface can be estimated via the limit layer theory as $F=0.664\rho^{0.5}U_{\infty}^{1.5}\sqrt{\mu L}\sim 10^{-3}N$ [9], which is much smaller than the dissipative force $F_{\mu}=CU_{\infty}\sim 10^{3}$ N.

At time $t=0$ a central polygon is removed from the array and a hydrostatic force is applied to every side of any adjacent polygon in contact with the fluid. This force is of the form

$$\vec{F}_p = p(t)lh\hat{\mathbf{n}}, \tag{8}$$

where $p(t)$ is the pressure at time t, l is the length of the side in contact with the fluid, h is the fixed height of the fracture, and $\hat{\mathbf{n}}$ is a unitary vector normal to this side.

In a real hydraulic fracture process [3] the fluid is injected at a certain rate and the pressure at the well bottom increases until a crack shows up. So we may set an initially pressure high enough to break the first layer of rock. It is common in petroleum engineering to take the fracturing fluid pressure as the pressure of a hydraulic column [10] and, when the fracture begins to propagate, the height of this column—and hence the pressure—drops. This will drive us to the conclusion that an appropriate model for the pressure in time is

$$p(t) = \rho g h_0 - \rho g \frac{V(t)}{S} = p_0 - \rho g \frac{V(t)}{S}, \tag{9}$$

where p_0 is the initial pressure, g is the acceleration of gravity, S is the pipe cross section, and $V(t)$ is the volume (area in 2D) of the fracture. This form for the pressure takes into account the general mass conservation relation widely used in different models of hydraulic fracture [3].

In our two-dimensional case, the volume (area) and superficial area (perimeter) of the fracture are found by identifying the points that are vertices of the fracture. The perimeter is the sum of the distances between each pair of adjacent vertices and the area is evaluated as $\frac{1}{2}(\Sigma_i x_i y_{i+1} - x_{i+1} y_i)$ for the set of vertices (x_i, y_i).

The initial results that we will show consider this simple model for the fluid and focus on some of the geometrical aspects of the hydraulic fracturing process. However in Sec. V we will include the effect of porous flow and reproduce the entire fracturing treatment.

IV. RESULTS IN ABSENCE OF FLUID LOSS

Despite the fact that the simulation is in two dimensions, our main objective is to simulate the hydraulic fracture as close to reality as we can. So, we chose simulation parameters that correspond to an average oil reservoir [3] and a real solid material [5]. They are summarized in Table I.

In a previous work [11], Tzschichholz and Herrmann computed the fractal dimension of the fracture in absence of tectonical stresses by using squares (instead of polygons) that obey the same interparticle forces that we used. Using a network of 150×150 squares, they found the fractal dimension for the perimeter. However, the squares were exactly equal, and hence the cohesive forces between elements would be the same. In order to introduce certain degree of randomness they used a statistical power-law distribution for the breaking threshold of the beams with an exponent r. They found that fractal dimension heavily depends on this exponent, reporting two distinct values: 1.44 for $r=-0.7$ and 1.39 for $r=-0.4$. Our model is different since the three breaking thresholds are the same for every pair of polygons [Eq. (4)], but the cohesive force depends on the length of the side shared by them. This results in a more realistic distribution for the breaking points.

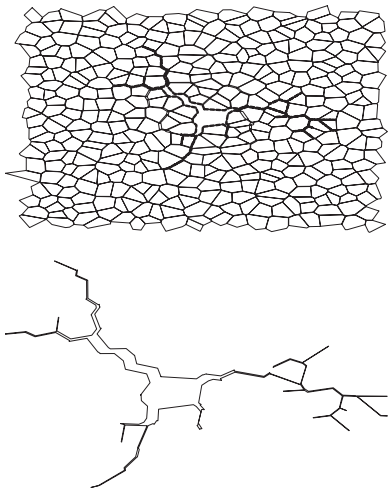

FIG. 4. (Top) The fracture obtained in the 20×20 polygon array without tectonical stresses. (Bottom) The fracture alone.

As a first test for our algorithm, we wanted to compute the fractal dimension for a fracture in absence of tectonical stresses and compare it with the results of Ref. [11]. Figure 4 shows the results for the fracture propagation over a 20×20 polygon array without external stresses and an initial fluid pressure of 47 MPa. As expected, the principal direction of fracture propagation is not well defined and the fracture shows a fractal structure. The simulation stops when the fracture reaches a certain value for the volume. Figure 5 shows the computation of this fractal dimension by using the box counting algorithm [12]. It shows a power-law dependence on two and one-half scales, with a slope of $d=1.223(40)$ and correlation coefficient $r^2=0.9873$. Despite the fact that a simulation with polygons requires considerably less number of bodies than a simulation with squares or disks in order to give the same results, this discrepancy can be a consequence of a low number of polygons. Figure 6 shows the dependence on the fractal dimension with the number of polygons employed to model the rock. It can be observed that the fractal dimension grows with the number of polygons, but it is still far from the value reported by Tzschichholz and Herrmann. This suggests to us that both the polygon shape and the different approach to establish the breaking thresholds may influence the fractal dimension of the fracture.

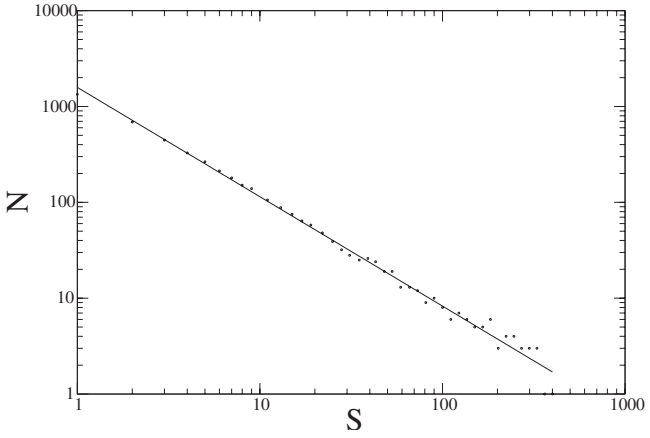

FIG. 5. Computation of the fractal dimension for the fracture perimeter in Fig. 4. The fractal dimension is the exponent of the relation between the minimum number of covering boxes (N) and the size of each box (s).

The next step is to compute the evolution in time for the fracturing pressure and the two main fracture dimensions: the area and perimeter for a system without tectonical stresses. We show the results of these calculations in Fig. 7. Without external stress, the pressure of the fracturing fluid decreases and, eventually, reaches the equilibrium with the granular and elastic forces (13 MPa). We can see sudden drops in the pressure due to the internal breaking of the cohesive beams. The area shows a similar behavior with sudden increments in time. But it is in the evolution of the perimeter where these strong changes become evident. Every step in this graph indicates a broken beam. Initially, when the beam is broken, the two polygons are still close enough to ensure that the area between them is very small, but the perimeter is not. This is why the perimeter shows rough increments whereas the pressure and area show a more continuous behavior. The internal equilibrium is the sign that the petroleum engineer expects in order to consider that the

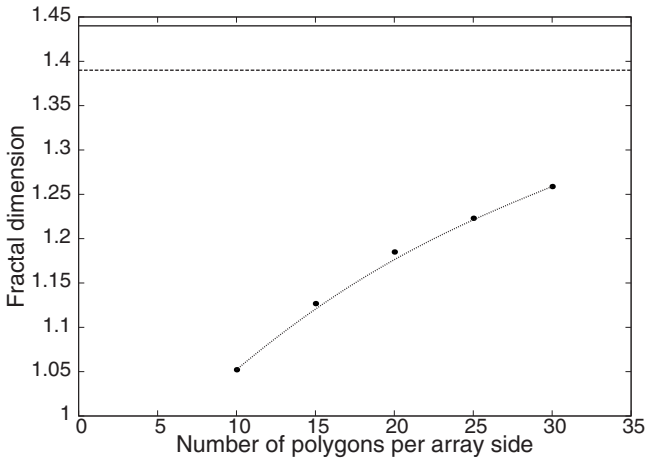

FIG. 6. Fractal dimension versus the size of the squared array of polygons employed. The two values reported for an array of 100 $\times$ 100 squares in Ref. [11] (1.44 and 1.39) are shown as a horizontal line for comparison.

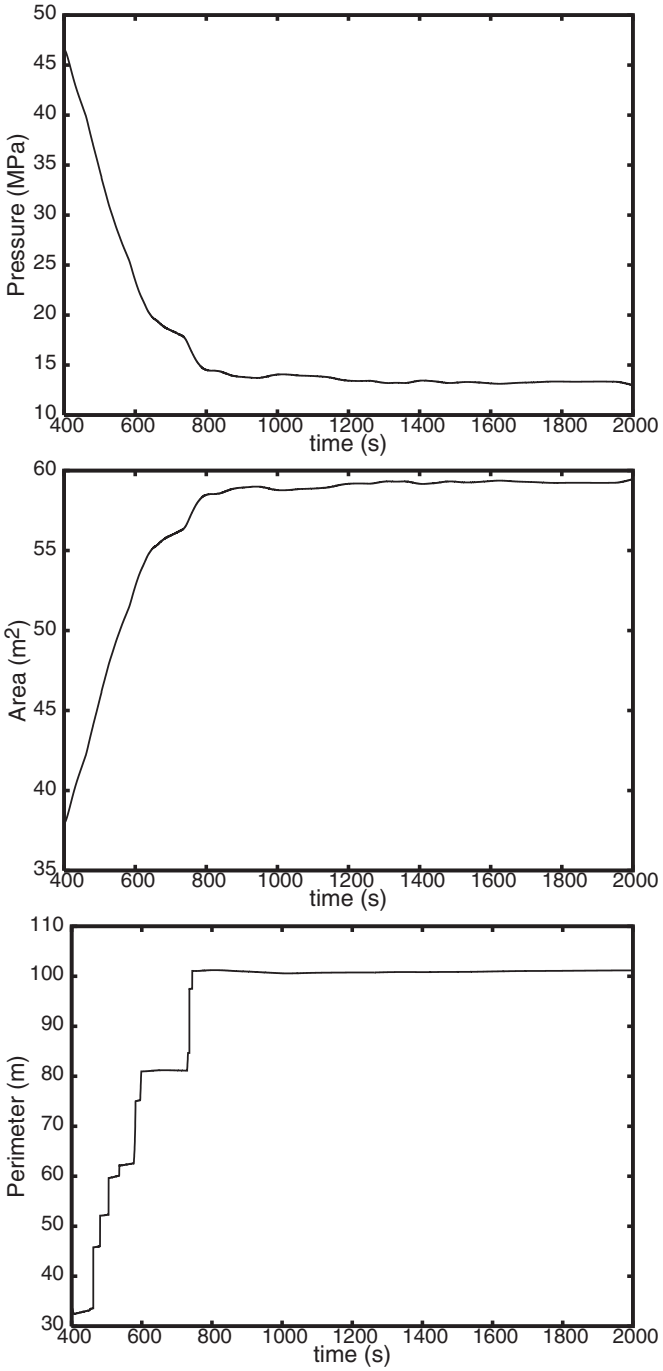

FIG. 7. (Top) The evolution of the fluid pressure, (center) the fracture area, and (bottom) the perimeter in absence of external stresses for the fracture of Fig. 4.

treatment is finished. In our simulation this equilibrium is reached in about 20 minutes, which is an accurate estimate of the duration of the real process (estimated times range from 15 minutes to 1 hour [10,1]).

We now want to observe the evolution of the crack under external stresses. With this idea in mind, we start from the same initial configuration of polygons with a constant stress along the y axis of 34.5 MPa and three different values (34.5, 69, and 103.5 MPa) of stress along the x axis. The results are shown in Fig. 8 for an array of 25 $\times$ 25 polygons. The simu-

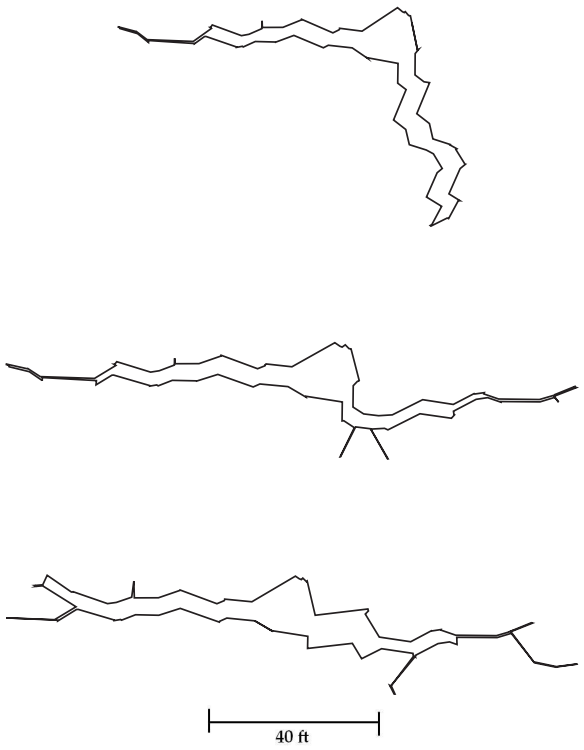

FIG. 8. Three different fractures for tectonical stresses of 34.5 MPa along the y axis and the values of (top) 34.5, (center) 69, and (bottom) 103.5 MPa for the stress along the x axis.

lation stops when the pressure equilibrium is reached.

As can be seen in the figure, when the two principal stresses are equal, the direction of propagation is almost random. The breaking rules ensure that the cracks will happen with higher probability in the beams with smaller cross sections (i.e., between polygons that share a short side) since the thresholds for beams have a value of 1% of strain and shorter cross sections will reach this value easier. This is the governing rule for the fracture in this stress regime. When the difference of the two principal stresses increases, the fracture takes the direction of the x axis (i.e., perpendicular to the minimum stress). This is a well known feature in geomechanics [13].

For the last case [103.5 MPa of stress along the x axis Fig. 8 (bottom)] we show in Fig. 9 the corresponding pressure, area, and perimeter in time. The simulation starts with an initial pressure of 103.5 MPa and reach an equilibrium at 44.5 MPa, almost 34.5 MPa above the equilibrium value for the stress-free case (Fig. 7). This difference is due to the closing effect of the minimum stress. The final area is 111.2 m^2 so, with our fixed height of 0.3 m, the final volume is therefore 33.4 m^3.

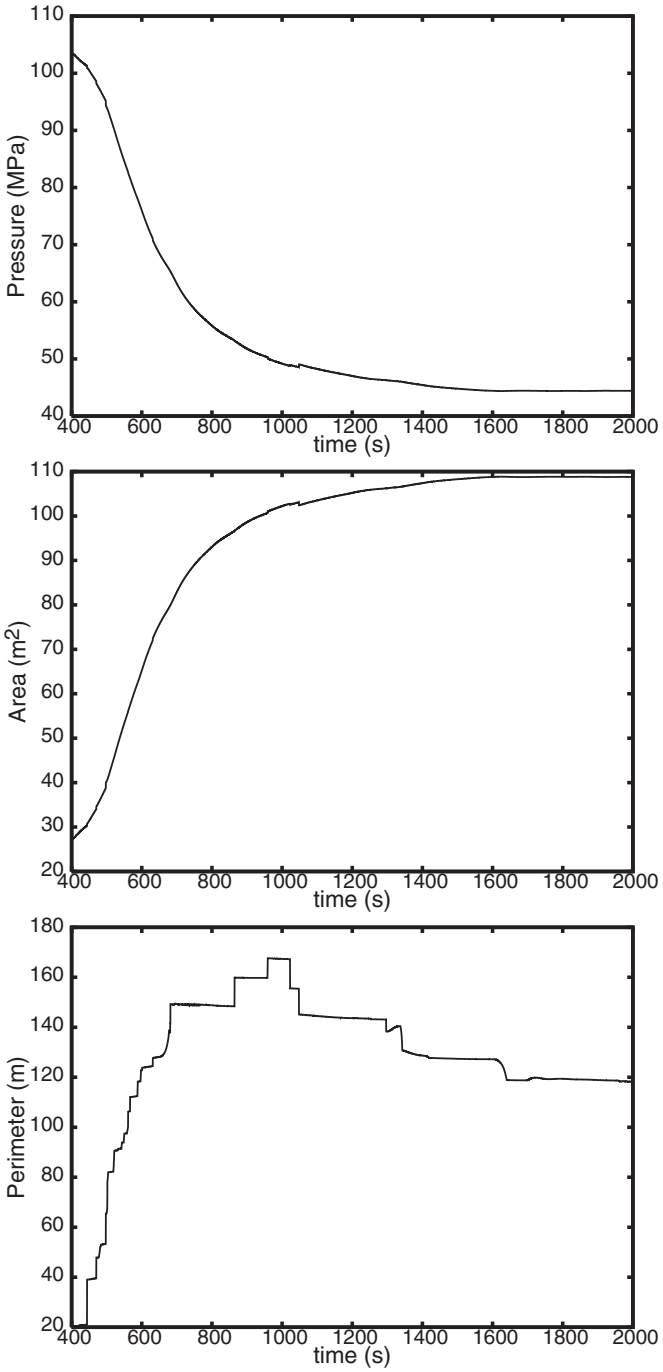

FIG. 9. (Top) The evolution of the fluid pressure, (center) the fracture area, and (bottom) the perimeter in the presence of external stresses for the fracture of Fig. 8 (bottom).

V. EFFECT OF THE RESERVOIR PERMEABILITY

Although Eq. (9) describes well the decreasing behavior for the pressure and its final equilibrium, it does not consider losses of the fracturing fluid due to the permeability of the reservoir. In this section we will introduce this effect, and therefore we must obtain the pressure in the entire reservoir. We begin with the well-known continuity equation,

$$\nabla \cdot \mathbf{J} + \frac{\partial \rho}{\partial t}, \tag{10}$$

where $\mathbf{J}$ is the fluid density and ρ is the fluid density. Also from Darcy's law [9] we know that the flux's density $\mathbf{J}$ of the

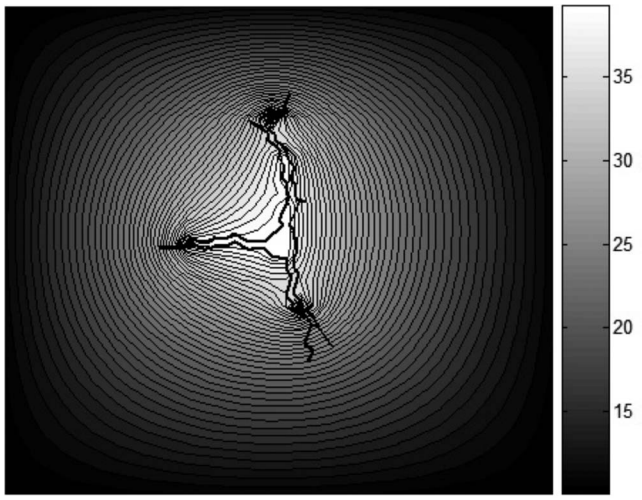

FIG. 10. Pressure (in MPa) at any point of our array of polygons for a particular step of time.

fluid is related with the permeability of the medium k and the viscosity μ, as follows:

$$\mathbf{J} = -\frac{k}{\mu}\nabla p. \tag{11}$$

Assuming an incompressible fluid and uniform values of permeability and viscosity, one obtains the well-known Laplacian equation for the pressure, p,

$$\nabla^2 p = 0. \tag{12}$$

We solved this equation by using the finite difference method. The boundary conditions for the pressure were, first, the value given by Eq. (9) for inside the fracture and, second, a constant value of 6.9 MPa in the edge of our array (which is a common value for the liquid pressure in oil reservoirs [3]). The results are summarized in Fig. 10.

We may estimate the efficiency of the process with our simulation by computing how much fluid was lost due to the rock's permeability, V_{lost}. From the pressure values computed from Eq. (12), we compute, first, the pressure gradient and, hence, the flux density from Eq. (11), with typical values for the permeability and viscosity (5 md and 1×10^{-3} Pa s, respectively [10]). Integrating the flux density over the perimeter (superficial area) we obtain the amount of fluid lost in a time interval Δt,

$$\frac{\Delta V_{\text{lost}}}{\Delta t} = \oint \mathbf{J} \cdot d\mathbf{s}. \tag{13}$$

The volume V_{lost} of fracturing fluid that is lost in the process is computed by summing up ΔV_{lost} for all time intervals.

The model for the whole process is completed by introducing new terms in Eq. (9) for a constant fluid injection rate, q, as

$$p(t) = \rho g \frac{qt - V(t) - V_{\text{lost}}(t)}{S}, \tag{14}$$

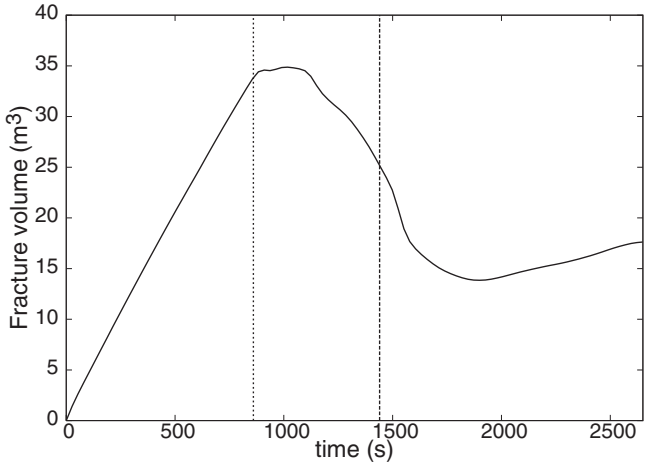

FIG. 11. Fracturing fluid pressure as a function of time for a simulation on an array of 25×25 polygons with a constant injection rate $q = 0.0069$ m^3/s and the parameters of Table I. Vertical lines divide the process into three stages.

The pressure obtained with this model for a 25×25 polygon array is shown in Fig. 11. One can observe the expected behavior of Fig. 1: its value increases until the surrounding rock breaks and the fracture begins to propagate. As can be seen in Fig. 11, the pressure reaches the equilibrium value shown in our previous simulations. Figure 12 (top) shows the lost volume rates and (center) the fracture volume for the same run. One can observe three different stages. In the first stage (0–860 s), lost rates are small, the pressure grows linear in time and the fracture grows without cracks at a constant rate, i.e., the fluid injection rate, q. In the second one (860–1400 s), the rock cracks, the pressure drops, and the lost volume rate grows. In the last one (1400–2600 s), the rock barely brakes, the pressure stabilizes, and the lost volume rate approximately equals the injection rate. In addition [Fig. 12 (bottom)], we observe at this last stage that the fracture volume grows as a power law of time with exponent $n = 0.587(6)$ (regression coefficient $r^2 = 0.9858$).

This gives us an excellent opportunity to compare our results with the classical PKN model [2], which assumes the fracture as an ellipse. In this model the efficiency of the fracture is defined as

$$\eta = \frac{V_{\text{injected}} - V_{\text{lost}}}{V_{\text{injected}}}. \tag{15}$$

For an efficiency close to 1 (no losses) there are two formulas for the evolution of the major and minor axes (L and w, respectively) as a function of time, t, for the cylindrical ellipse [1] and a given fixed height, h_f [14,15],

$$L(t) = 0.39\left(\frac{Gq^3}{\mu h_f^4}\right)^{1/5} t^{4/5}, \tag{16a}$$

$$w(t) = 2.18\left(\frac{\mu q^2}{G h_f}\right)^{1/5} t^{1/5}, \tag{16b}$$

where G is the shear Young modulus, q is the injection rate, and μ is the fracturing fluid viscosity, as before. The volume

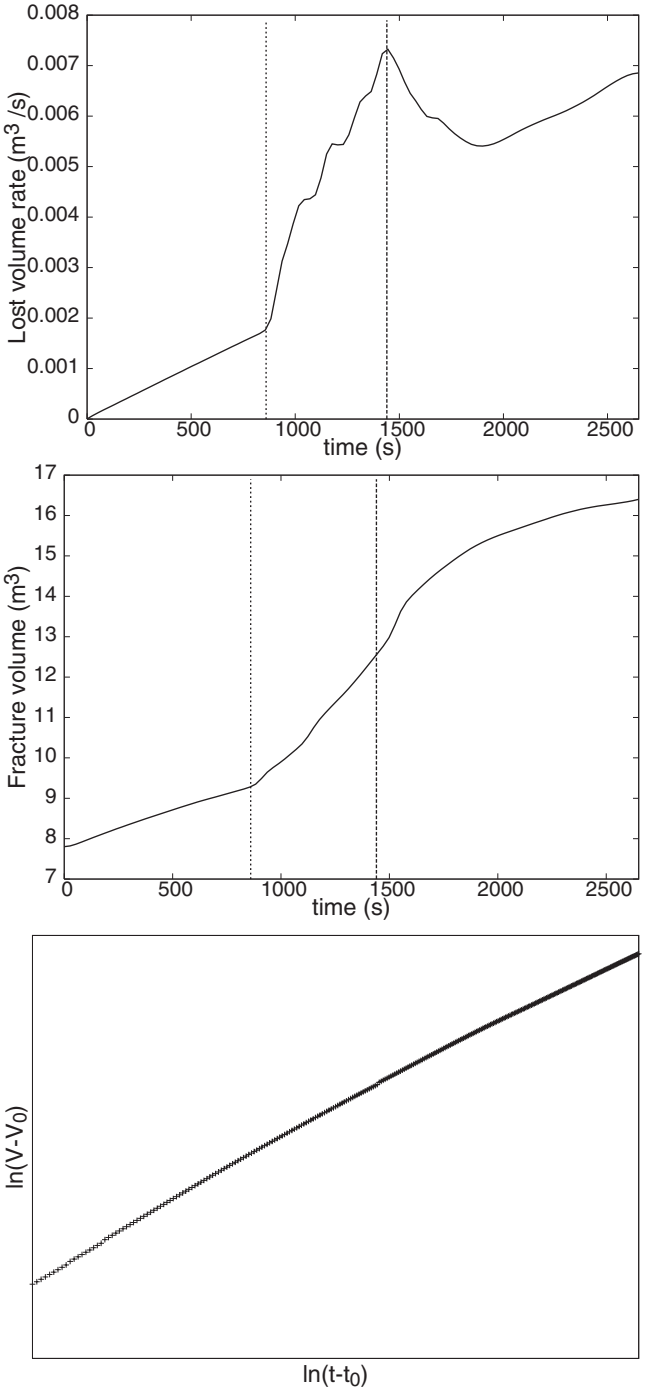

FIG. 12. (Top) Rate of lost fluid, (center) fracture fluid, and (bottom) fracture volume at the final stage (from 1600 s) in log-scale showing a possible power law. $t_0=1600$ s and V_0 is the volume at this time. The curves are from the same simulation as Fig. 11.

of the cylindrical ellipse, $V=\pi h_f L w$, grows linearly with time as $V(t)=qt$ and all the fluid injected goes to the fracture at this maximum efficiency. In Fig. 11 we can see that initially (stage 1) the volume grows linearly in time but its slope suddenly increases when the rock fractures (stage 2). This is not the linear behavior of the PKN model at high efficiencies. The PKN model assumes that the fracture begins immediately after the fluid is injected. In contrast, our model assumes that certain threshold should be met before the fracture begins to propagate and once this threshold is reached the volume grows faster. This is the origin of the discrepancy between both models.

At low efficiencies ($\eta \to 0$), we have a similar set of equations for the ellipse major and minor axis,

$$L(t) = \frac{qt^{1/2}}{2\pi h_f C_L}, \tag{17a}$$

$$w(t) = \left(\frac{\mu q^2}{\pi^3 G C_L h_f}\right)^{1/4} t^{1/8}, \tag{17b}$$

where C_L is the so-called leak-off coefficient. Now the volume grows slower, $V \propto t^{5/8}$, due to the heavy losses. Our model shows by the end of the simulation (stage 3) an efficiency of 19%, that appears in the high-loss regime. The power-law dependence we found in this region gave us an exponent $n=0.587(6)$, close to the exponent found with the analytical PKN model. Of course, our model is far more realistic since it does not assume neither any particular form for the fracture nor any efficiency state from the beginning. Instead, it gives the efficiency of the whole treatment as a result.

VI. CONCLUSIONS

We have introduced a model for the hydraulic fracture process of the petroleum industry using a discrete element method which takes into account the elastic behavior of the rock and the Mohr-Coulomb criterion for the fracture appearance. The rock is modeled as an array of Voronoi polygons joined by elastic beams, and it is forced by the tectonical stresses and the hydrostatic pressure of the fracturing fluid. This pressure is modeled, in turn, like an hydraulic column. When the fracture volume starts to increase, the column height, and hence the pressure, decreases.

Our simulation shows that the fracturing pressure reaches an equilibrium in a time which is comparable with the usual required time for the real process. It also reproduces the expected behavior for the fracture propagation under external stress, i.e., that the fracture goes along the direction of the maximal stress. Our model can also take into account the rock permeability by solving at every time step the Darcy's law by finite differences and computing the rate of fluid volume that is lost into the rock due to this permeability. When this last effect is included, our simulation reproduces the expected behavior for the pressure.

When the lost fluid volume is taken into account, our simulation shows three different stages for the fracturing process. In the first one, the pressure grows linearly with time, losses are small, and the fracture volume grows with the injection rate. In the second stage, the rock starts to break, the pressure drops, and the volume fracture grows faster than linear. In the third stage the pressure stabilizes, the rock barely breaks, and the fracture volume grows with a power-law dependence of time. The exponent we found for this last stage, $n=0.587(6)$, is close to the one predicted by the clas-

sical PKN model [2], which assumes an elliptical shape for the fracture.

In absence of tectonical stresses, our model gives fractal dimensions for the perimeter between 1.052 and 1.259, growing with the number of polygons employed but still far from the values of 1.44 and 1.39 reported for similar models with squares and power-law distributions of the breaking thresholds [11]. In contrast, breaking thresholds in our model are the same for all polygons, but cohesive forces depend on the length of the common sides between polygons. This suggests to us that the fractal dimension may be also modified by the polygon shape and the details of the breaking law.

Of course, our model is just a preliminary study. Further analysis should include a more realistic model for the fluid, since we have taken a constant pressure along the entire fracture and the real pressure depends on the distance from the injection point. The real fluid also provides shear stress on the rocks due to its viscosity and not only normal stress, as we assumed. Of course, there are many other factors, like the three-dimensional propagation of the fracture, which should be considered in order to make an accurate simulation of this widely used process. Nevertheless, these microscopical models are good alternatives to classical models, like PKN. Our computer model runs in a 1.8 GHz Athlon XP PC in an approximate time of 6 hours, i.e., it can be implemented with very modest computational resources. This may open new opportunities for the development of similar micromechanical models for industrial applications.

We expect that the development of microscopic simulation models as the one introduced here will contribute to both the computational physics and the petroleum industry. Actually, simulators that can run in portable PCs, are greatly appreciated by the petroleum engineers for a quick guide in the early stages of the hydraulic fracture process, and we hope that this work can contribute to the future development of such professional simulators.

ACKNOWLEDGMENTS

The authors would like to thank Professor Hans J. Herrmann and Professor Jose Gildardo Osorio for useful discussions. This work was supported by the Foundation for the Advance of Science of the Bank of the Republic of Colombia (Contract No. 1838) and the Research Vice rector office of the National University of Colombia (Contract No. 20201006052).

[1] M. Economides, *Reservoir Stimulation* (Wiley, New York, 2000).
[2] W. S. Lee, Lagrangian formulation for penny shaped and Perkins Kern geometry models, SPE formation evaluation, 1989.
[3] K. Ben-Naceur, *Modelling of Hydraulic Fractures* (Dowell, Schlumberger, 1995).
[4] F. Kun, arXiv:cond-mat/9512017.
[5] F Kun, Int. J. Mod. Phys. C **7**, 837 (1996).
[6] Prediction of sand erosion in process and pipe components, edited by J. P. Brill and G. A. Gregory, BHR group Conference Series, No. 31, pp. 217–227.
[7] D. C. Rapaport, *The Art of Molecular Dynamics* (Cambridge University Press, Cambridge, 1995).
[8] L. Verlet, Phys. Rev. **159**, 98 (1967); **165**, 201 (1967).
[9] M. C. Potter and D. C. Wiggert, Mechanics of fluids, 3rd ed., Brooks/Cole Editorial, 2001.
[10] R. E. Jonhson and C. W. Gustafson, Phys. Fluids **31**, 3180 (1988).
[11] F. Tzschichholz and H. Herrmann, Phys. Rev. E **51**, 1961 (1995).
[12] A. Bunde and S. Havlin, *Fractals and Disordered Systems* (Springer-Verlag, Berlin, Heidelberg, 1996).
[13] L. C. Murdoch, J. Geotech. Geoenviron. Eng. **128**, 479 (2002).
[14] J. Adachi *et al.*, Int. J. Rock Mech. Min. Sci. **44**, 739 (2007).
[15] F. Tzschichholz and M. Wangen, *Modelization of Hydraulic Fracture in Porous Materials. Advances in Fracture Mechanics* (WIT, Southhampton, 1999), pp. 227–261.